FINITE ELEMENT ANALYSIS OF TOP-CASING ELECTRIC SOURCE METHOD FOR IMAGING HYDRAULICALLY-ACTIVE FRACTURE ZONES

LIST OF AUTHORS:

Evan Schankee Um, Earth and Environmental Sciences Area, Lawrence Berkeley National Laboratory, evanum@gmail.com and esum@lbl.gov

Jihoon Kim, Harold Vance Department of Petroleum Engineering, Texas A&M University, jihoon.kim@tamu.edu

Michael J. Wilt, Earth and Environmental Sciences Area, Lawrence Berkeley National Laboratory, mwilt@lbl.gov

Michael Commer, Earth and Environmental Sciences Area, Lawrence Berkeley National Laboratory, mcommer@lbl.gov

Seung-Sep Kim, Department of Geology and Earth Environmental Sciences, Chungnam National University, Daejeon, South Korea, seungsep@cnu.ac.kr

ABSTRACT

Imaging hydraulically-active fracture zones (HAFZ) is of paramount importance to subsurface resource extraction, geological storage and hazardous waste disposal. We present advanced 3D finite-element (FE) electrical imaging algorithms for HAFZ in the presence of a steel-cased well. The algorithms employ tetrahedral FE meshes in the simulation domain and coarse rectangular finite-difference (FD) meshes in the imaging domain. This heterogeneous dual-mesh approach is well suited to modeling multi-scale earth model due to steel-cased wells. We show that the algorithms accurately and efficiently simulate surface electric field measurements over a 3D HAFZ at depth when one end point of a surface electric source is connected to a wellhead. For brevity, this configuration is called the top-casing electric source method. By replacing a hollow cased well with a solid prism, we improve our computational efficiency without affecting the solution accuracy. The sensitivity of the top-casing source method to HAFZ highly depends on the continuity of a steel-cased well, because it makes currents preferentially flow to HAFZ. The sensitivity also depends on conductivity structures around the well because they control current leaking from the steel-cased well. We show that the method can image a localized HAFZ and detect changes in its width and height. The imaging results are improved when a volume of the imaging domain is constrained from geomechanical perspectives. A primary advantage of the method is the fact that both sources and receivers are placed on the surface, thus not interrupting well operation.

INTRODUCTION

Imaging hydraulically active facture zones (HAFZ) is an important topic in applied geophysics. For example, hydraulic fracturing and stimulation have been widely used for enhancing production in oil, gas and geothermal fields (Zoback 2007; Zoback et. al. 2010). Traditional borehole methods are sensitive to deep HAFZ, but their sensitivity is often limited to the vicinity of the well. Thus, they cannot tell us about an overall hydraulically stimulated volume of subsurface. The most often used method for characterizing HAFZ in a reservoir scale would be micro-earthquake (MEQ) methods (Warpinski et al. 2005; Vermylen and Zoback, 2011). By analyzing MEQ event locations, we can estimate the stimulation volume. However, MEQ-based mapping highly depends on initial velocity models, which we do not know well, leaving uncertainties. More importantly, MEQ event locations do not necessarily correlate with active fluid pathways and thus, provide only a portion of the answer about estimating overall HAFZ (Hoversten et al, 2015).

It is also important to image deep HAFZ in geological storage sites such as CO_2 sequestration and hazardous waste disposal sites. During their injection phase, MEQ events are often recorded and can be utilized for imaging fluid movements and monitoring potential leakage. However, after the injection phase, the magnitudes of MEQ are often too small to be reliably recorded and interpreted in practice (Johnston and Shrallow, 2011). Active-source seismic methods can also be considered an effective tool for the monitoring goal. However, their major limitation is long acquisition time and high processing cost.

Electrical and electromagnetic (EM) methods are sensitive to pore fluids and thus have the potential to directly sense a HAFZ, complementing MEQ and active source seismic monitoring. To ensure the sufficient sensitivity of the methods to deep HAFZ, one can consider injecting highly-conductive saline fluid or fluid with electromagnetically contrasting tracers (e.g. Moridis and Oldenburg, 2001; Rahmani et al., 2014; Kim et al., 2014). Such fluid and tracers can raise the magnitude of weak anomalous signals from HAFZ to a detectable level. It is also proposed to use a steel-cased well as a boosting electric source that directly charges HAFZ (Schenkel and Morrison, 1994; Marsala et al., 2014; Commer et al., 2015; Hoversten et al., 2015; Um et al., 2015; Patzer et al., 2017). The sensitivity analysis of the approaches proposed above has been numerically carried out with simple inflated fracture geometries (Weiss et al., 2016).

In this paper, we numerically evaluate a surface-based electrical method with a steel-cased well for detecting and imaging HAFZ. In our survey configuration, one end point of a surface electric dipole source is connected to the top of a steel-cased well to directly charge HAFZ around the well. The other point of the electric dipole source is grounded sufficiently away from the cased well. The electric fields are measured on the surface. For simplicity, we call this configuration the top-casing electric source method. The potential advantage of the method is to characterize HAFZ without requiring well intervention because both sources and receivers are placed on the surface. This advantage makes the proposed electrical method fast and economic in hydraulic fracturing operations and safe in hazardous waste disposal sites.

The remainder of this paper is organized as follows. First, we describe a 3D finite-element forward and inverse modeling algorithm for the electric resistivity method in the presence of a steel-cased well. To handle the multi-scale DC modeling associated with the presence of the steel-cased well, we introduce a dual-mesh-based algorithm that utilizes structured finite-difference (FD) imaging meshes and unstructured finite-element (FE) simulation meshes. The effectiveness of the dual-mesh approach for modeling a steel-cased well is discussed. Second, we present a simplified version of a steel-cased well model and show its accuracy and efficiency. Third, using the algorithms, we evaluate the detection sensitivity of the top-casing electrical source method for several simple 3D HAFZ. Finally, we show the imaging sensitivity of the method through inversion experiments as the final proof-of-concept analysis step.

FORWARD MODELING OF 3D ELECTRICAL RESISTIVITY METHOD

In this paper, we employ a 3D FE electrical resistivity modeling algorithm described in Um et al. (2010). The governing equation of the electric resistivity method is given as Poisson's equation

$$\nabla \cdot (\sigma(\mathbf{r})\, \nabla \phi(\mathbf{r})) = -\nabla \cdot \mathbf{j}_s(\mathbf{r}), \qquad (1)$$

where $\phi(\mathbf{r})$ is a potential at position $\mathbf{r}$, $\sigma(\mathbf{r})$ is electrical conductivity, and $\mathbf{j}_s$ is an electric source.

We discretize the computational domain with tetrahedral meshes. To develop the weak statement, equation 1 is multiplied by a weighting function $\omega(\mathbf{r})$ and is integrated over the volume of a tetrahedral element, resulting in

$$\iiint_{V^e} \omega^e(\mathbf{r})\nabla\times(\sigma^e(\mathbf{r})\nabla\phi^e(\mathbf{r}) + \nabla\times\mathbf{j}_s(\mathbf{r}))dv = 0, \qquad (2)$$

The superscript *e* indicates the e^th^ tetrahedral element. V^e is the volume of the eth tetrahedral element. The unknown potential at **r** inside the eth element is interpolated using the set of four Lagrange polynomials $n_i^e(\mathbf{r})$ (Jin, 2015)

$$\phi^e(\mathbf{r}) = \sum_{i=1}^{4} \phi_i^e n_i^e(\mathbf{r}), \qquad (3)$$

where ϕ_i^e is the potential at the ith node of the eth element.

We also use the same Lagrange polynomials as the weighting function $\omega(\mathbf{r})$ in equation 3. Thus, substituting equation 3 into equation 2 and replacing $\omega(\mathbf{r})$ by $n_i^e(\mathbf{r})$ result in

$$\mathbf{M}^e\mathbf{u}^e = \mathbf{s}^e \qquad (4)$$

,where

(*i*,*j*) element of $\mathbf{M}_{ij}^e = \iiint_{V^e} \sigma^e(\mathrm{r})\left(\frac{\partial n_i^e}{\partial x}\frac{\partial n_j^e}{\partial x} + \frac{\partial n_i^e}{\partial y}\frac{\partial n_j^e}{\partial y} + \frac{\partial n_i^e}{\partial z}\frac{\partial n_j^e}{\partial z}\right)dV$, (5)

i element of $\mathbf{u}^e = [\phi_1^e \quad \phi_2^e \quad \phi_3^e \quad \phi_4^e]$, (6)

i element of $\mathbf{s}^e = \iiint_{V^e} n_i^e(\mathbf{r})\nabla\times\mathbf{j}_s(\mathbf{r})dv$, (7) Equation 4 is considered local because it comes from each tetrahedral element. Using the node connectivity information, local matrix equations from individual elements are assembled into a single global matrix equation.

The resulting system of FE equations is symmetric positive definite. Note that the system matrix is typically ill-conditioned because the contrast in conductivity across the air-casing interface can be larger than ten orders of magnitude and also because the discretization of a hollow cased well in a deep earth model requires mixing millimeter-scale elements with kilometer-scale ones (Um et al., 2015). Our choice of numerical linear algebra for equation 4 is sparse Cholesky factorization and subsequent backward and forward substitution (Davis, 2006). After the total potential is determined at each tetrahedral node, the potential difference at two arbitrary end-points of a finite-long electric dipole receiver is interpolated and divided by the length of the receiver.

INVERSE MODELING ALGORITHM WITH STEEL-CASED WELL

Our inversion implementation described here is based on a general frequency-domain EM inversion framework. An objective functional is given as

$$\Phi = [\mathbf{D}(\mathbf{d}_{\text{obs}} - \mathbf{d}_{\text{pred}})]^T [\mathbf{D}(\mathbf{d}_{\text{obs}} - \mathbf{d}_{\text{pred}})] + \lambda (\mathbf{W}\boldsymbol{\sigma})^T (\mathbf{W}\boldsymbol{\sigma}) , \qquad (8)$$

where $\mathbf{D}$ is a data weighting matrix, $\mathbf{d}_{\text{obs}}$ and $\mathbf{d}_{\text{pred}}$ are observed and predicted DC data, respectively, $\mathbf{W}$ is a regularization matrix defined by FD approximation to Laplacian operator, and $\boldsymbol{\sigma}$ is a conductivity model. λ is a regularization parameter.

Our inversion algorithm employs a limited-memory Broyden–Fletcher–Goldfarb–Shanno (L-BFGS) algorithm (Nocedal and Wright, 2006). Inside L-BFGS, a Cholesky factor for equation 4 is re-used to compute a search direction vector. Accordingly, one inversion iteration requires only one new factorization if the initial trial step satisfies sufficient decrease of Φ. If the trial step fails to sufficiently decrease Φ, a line search algorithm performs back-tracking. When multiple sources are used, they share the factored matrices. To prevent conductivity overshoots in the course of inversion, the conductivity model is bounded by a logarithmic transformation function (Newman and Alumbaugh, 2000).

To accurately and efficiently model a steel-cased well, our inversion scheme includes three characteristics. First, we use different meshes in the model and simulation domain. Note that dual mesh approaches have been widely used in EM imaging (Commer and Newman, 2008, Egbert and Kelbert, 2012; Yang et al., 2014; Grayver, 2015; Yang et al., 2016). However, our dual mesh approach is distinct from others since we use a dual mesh approach with heterogeneous mesh types. Coarse rectangular FD meshes are used to define the model space (i.e. FD model meshes), whereas fine tetrahedral FE meshes (i.e. FE simulation meshes) are used to compute forward solutions and subsequent gradient vectors. The motivation behind the FE-FD dual mesh approach is multifold. First, by using the tetrahedral FE simulation meshes, the simulation domain is highly refined inside and around wells but remains coarse elsewhere, leading to efficient forward modeling in the presence of wells (Um et al., 2015). This is a prime advantage of our FE-FD dual mesh approach over a traditional FD-FD dual mesh approach where local refinements in simulation meshes extend both horizontally and vertically. Second, it is practical to use rectangular FD meshes in the model domain. For example, visualization and analysis of tetrahedral meshes are cumbersome and daunting especially when millimeter scale elements for wells are mixed with kilometer scale elements for regional geology. Rapid and accurate display of large multi-scale tetrahedral meshes is currently an active research area in both earth sciences and computer sciences. In contrast, the use of the structured FD model domain allows us to easily and rapidly visualize and analyze EM imaging results even in the course of inversion. This is a major practical advantage of our FE-FD dual mesh approach over single mesh FE inversion approaches and FD-FD approaches.

Second, we define two mapping matrices that connect one meshes with the other meshes: $\mathbf{M}_{FE2FD}$ and $\mathbf{M}_{FD2FE}$ (Um et al., 2017). $\mathbf{M}_{FD2FE}$ is N_{FE}-by-N_{FD}, where N_{FD} and N_{FE} are the number of cells in the FD meshes and the number of tetrahedra in the FE meshes, respectively. Its (i,j) element is a ratio of an intersectional volume of the i^{th} FE element and the j^{th} FD cell to the volume of the i^{th} FE element. In contrast, $\mathbf{M}_{FE2FD}$ is a reverse operator of $\mathbf{M}_{FD2FE.}$ Its size is N_{FD}-by-N_{FE}. Its (*i*,*j*) element is a ratio of an intersectional volume of the i^{th} FD cell and the j^{th} FE element to the volume of the i^{th} FD cell. Therefore, $\mathbf{M}_{FD2FE}$ and $\mathbf{M}_{FE2FD}$ map $\boldsymbol{\sigma}$ from FD to FE and from FD to FE, respectively, being able to use heterogeneous mesh types in the model and simulation domain. More details on the two mapping matrices can be found in Appendix.

Third, after L-BFGS computes a search direction vector, $\mathbf{M}_{FE2FD}$ maps the vector from FE to FD. Before it is mapped to FD, its elements that correspond to the steel-cased wells are zeroed. The L-BFGS line search is performed in the FD model space to find a next conductivity model that decreases Φ. When a candidate FD model with a trial step length is formed, $\mathbf{M}_{FD2FE}$ maps the FD model to the FE simulation meshes. Note that the resulting FE model does not yet include the steel-cased well because the FD model in the model space does not include it. Therefore, at this point, the conductivity of the steel-cased well is assigned to the FE elements. Accordingly, the FD model space does not have fine grids for the steel-cased well but remains coarse, which is important for stable electrical resistivity imaging with a limited number of electrode receivers. In contrast, the FE modeling uses fine meshes, includes the steel-cased well, and accurately simulates EM responses to the wells. The implementation steps for our inversion are summarized below.

(1) Choose a starting FD/FE model.

(2) If it is a FD model, map it from FD to FE space using $\mathbf{M}_{FD2FE}$ and add prescribed cased wells to the FE model.

(3) Perform forward modeling and gradient calculation for the current model in the FE space by solving equation 4.

Repeat:

(4) L-BFGS determines a search direction vector.

(5) Set elements of the vector that correspond to the cased well to zero.

(6) Map the vector from FE to FD space using $\mathbf{M}_{FE2FD}$.

    Repeat:

    (7) Create a candidate FD model with a trial step length.

    (8) Map the candidate model from FD to FE using $\mathbf{M}_{FD2FE}$ and add the cased well to FE.

    (9) Perform forward modeling and gradient calculation for the candidate model in the FE space.

    (10) If Φ does not sufficiently decrease, choose a new trial step length.

    Until Φ sufficiently decreases

Until stop criteria for inversion are met

MODELING OF TOP-CASING ELECTRIC SOURCE METHOD

The FE forward modeling algorithm with a direct solver has been proven accurate for computing electric and EM responses to an earth model that features small-scale geometry and extreme conductivity contrast of a steel-cased well (Commer et al., 2015; Um et al., 2015). Fine tetrahedral meshes are used to accurately discretize arbitrarily complex fracture and well geometries and coarse meshes elsewhere. However, the direct discretization of multiple long (e.g. a few kilometers) hollow cased wells requires a number of tiny elements (e.g. a few ten million unknowns). Thus, modeling complex well structures with direct solvers is often prohibitively expensive. In most cases, the direct FE discretization is useful for generating reference responses to a cased well but is not practical enough for inverse modeling where a number of forward modeling needs to be completed.

To practically model a steel-cased well in the 3D Cartesian coordinate system, several approximation approaches have recently been proposed. For example, a hollow well can be approximated with a prism

(Weiss et al., 2015; Puzyrev et al., 2016). Its conductivity value is determined such that the cross-sectional conductance of the prism is kept same as the hollow well. The well can also be replaced with a series of small electric dipoles along the well in the DC and frequency domain (Cuevas, 2014; Nieuwenhuis et al., 2015). Weiss (2017) introduces a hierarchical electrical conductivity model for representing complex steel infrastructures and fractures at low computational cost. The accuracy of the approximation methods depends on various factors including background geology, source types and frequencies, well completion designs and distribution, distances between wells, sources and receivers and others. Therefore, one needs to use an approximation method in its scope and compare approximate solutions with reference solutions.

Of the approximation methods above, our choice is to replace a hollow steel-cased well by a prism. Before we present detection and imaging sensitivity of the top-casing electric source method to HAFZ in the next sections, we first show its accuracy and effectiveness in the scope of our modeling problem. As shown in **Figure** 1, the size of a prism is set to the outer diameter of the casing. We use the mesh-generating software, TetGen (Si, 2015) to generate tetrahedral meshes. **Figure** 2 shows that the two models produce nearly identical responses. The relative differences between the hollow steel-cased well and the prism rapidly decrease with increasing distance from the wells. This indicates that the detailed geometry of the well's outer surface becomes less important as a receiver position becomes distant from the well. After the replacement, the number of elements reduces from 8,421,559 to 745,151 elements, showing the effective reduction in modeling problem size without affecting the solution accuracy. Equation 4 for the model shown in **Figure** 1b is solved in about 3 minutes using 3.40GHz Intel Skylake processor, which is fast enough for forward and inverse modeling experiments in the next section.

In the next example, we consider a 1km long hollow steel-cased well and its corresponding cylinder and prisms. For independent verification, we compute surface electric DC responses with a Poisson solver that is embedded into the 3D FD time-domain modeling algorithm (Commer and Newman, 2004; Commer et al., 2015). Because FD and FE algorithms are different numerical solution approaches for the same physics, the agreement between FE and FD solutions will show not only the accuracy of our FE algorithm but also the validity of the prism approximation.

Figure 3 shows a cross-sectional view of 1) a 1km long hollow steel-cased well, 2) its corresponding solid cylinder and 3) rectangular prism. One end point of an 870m long electric dipole source is connected with the surface of the steel-cased well and its alternatives. The background conductivity is set to 0.0333 S/m. Their surface electric field responses are shown in **Figure** 4a. Their relative differences with respect to the hollow well model are plotted in **Figure** 4b. For comparison, we also compute the electric field responses to the rectangular prism model using the FE algorithm described in this manuscript. The resulting FD and FE solutions agree well with each other. For example, the hollow steel-cased well and the solid cylinder (both FD models) produce nearly identical responses. When the steel-cased well is replaced with the rectangular prism, some numerical errors are introduced, but they are sufficiently small (less than 1.5%). The relative differences between the hollow steel-cased well model and its FD cylinder and prism models decrease with increasing distance from the well. The FE solution to the rectangular prism also agrees well with the three FD solutions, showing both the accuracy of the FE modeling algorithm and the validity of the casing approximation approach in the scope of our modeling problem.

FORWARD SENSITIVITY OF TOP-CASING ELECTRIC SOURCE METHOD TO HAFZ

Figure 5 shows a top-casing electric source configuration used in this study where one end point of the electric source is directly connected to the well head and the other end point is grounded sufficiently distant (2km) from the well head. A 2km long array of *x*-oriented electric receivers is placed along the +*x* direction at y=0m (survey line 1) and a 4km long array of *y*-oriented electric receivers along the ±*y* direction at *x*=2km (survey line 2). We consider an L-shaped well for simplicity. The vertical part of the well is 1.6 km deep and the horizontal part 400 m long. The casing is $5 \cdot 10^6$ (S/m) conductive and its diameter is set to 0.3 m. The well is replaced to its equivalent rectangular prism discussed earlier.

Because of the high contrast of electrical conductivity between the prism and the background geology, the high concentration of the electrical current preferentially flows along the surface of the prism and directly charges HAFZ. We consider that the high-pressure injection of saline fluid creates HAFZ (Kim et al., 2014). HAFZ is created perpendicular to the horizontal well and 200m away from the vertical well. Note that this is a relatively shallow hydraulic fracturing model. Depths of fracturing operations range from 3 to 5 km (Fisher and Warpinski, 2012). Their lateral distance from the vertical well also varies from 1.6 to 5km. The deeper depth and longer lateral distance mean that anomalous responses to HAFZ can be significantly smaller than those shown here. Accordingly, they would be vulnerable to cultural noises. In such cases, one may need to consider downhole based methods presented in Hoversten et al. (2017). While we are aware of the challenging issues associated with deep fracturing problems, here we mostly focus on the relatively shallow problem as the basic feasibility study of the top-casing source electric method.

Figure 6 shows simple four HAFZ models considered in this study. Their dimensions are summarized in **Table** 1. Note that the fracture propagation is bounded within the overburden and underburden layers that have higher minimum horizontal stress and/or higher strength than those of the reservoir, propagating in a horizontal direction. The size and the shape of the HAFZ models above are comparable to those that can be determined by well-known analytic fracture models such as Khristianovic-Geertsma-de Klerk (KGD) and Perkins-Kern-Nordgen (PKN) fracture (Perkins and Kern, 1961; Geertsma and de Klerk, 1969; Nordgren, 1972; Daneshy, 1973; Gidley et al., 1990) and thus, honor basic geomechanics associated with fractures. As shown in **Table** 1, we do not consider directly modeling micro-scale facture networks. Rather, the thickness of the fracture networks is artificially inflated into 1m thick HAFZ in a volume-averaged sense as done in Weiss et al. (2015) and Hoversten et al. (2017). The inflation approach is geophysically reasonable when the low resolution of the electrical method and the distance between source/receiver and HAFZ are considered.

Before we present numerical modeling examples, we briefly discuss a noise floor. In active fracturing sites and oil fields, the noise floor may vary by several orders of magnitude. For example, Tietze et al. (2015) report that the noise floor of electric field measurements in a German oil field is about 10^{-10} V/m, which is subsequently considered a noise floor in Hoversten et al. (2107). It is also reported that the floor can often be close to 10^{-7} V/m. Therefore, to achieve a desired noise floor in practice, one must consider stacking data. For example, when the raw noise floor is 10^{-9} to 10^{-7} V/m, 100 to 1,000,000 stacking operations are required to achieve 10^{-10} V/m noise floor.

Figure 7 shows the electrical field measurements along survey line 1 and 2 over the four HAFZ models. The top-casing electrical source method clearly distinguishes between the four models. Their electric field amplitudes are larger than both optimistic and pessimistic noise floors discussed earlier. To highlight the role of the steel-cased well as a conduit for a high concentration of electric currents that charge HAFZ, we repeat the same modeling without the casing. **Figure** 8 shows that the electrical field measurements over the background model and the four models are nearly identical. The surface electrical method does not sense the presence of HAFZ. This modeling shows that steel-cased wells that have been regarded as a disturbance to electrical and EM geophysics can be beneficial for sensing deep localized targets when the wells responses can be accurately and efficiently modeled.

Next, we examine two factors that directly control the sensitivity of the electrical method to HAFZ. The first factor is the continuity of the steel cased well. **Figure** 9 shows the electric field measurements over three different continuity conditions: the intact casing, the corroded casing and the broken casing. To realize a corroded casing condition, we consider a 1m long low conductivity patch ($5 \cdot 10^{3}$ S/m) at z=500m. When the casing is completely broken, the 1m long patch has the conductivity of the background ($5 \cdot 10^{-3}$ S/m). As the continuity is deteriorated due to the corrosion, the method still distinguishes between the four HAFZ models but its sensitivity decreases. The complete break no longer allows the high concentration of electrical currents to efficiently flow along the casing and charge HAFZ, resulting in the complete loss of the sensitivity.

The conductivity of the background geology also plays an important role in controlling the overall sensitivity of the method. **Figure** 10 shows the electric field measurement along survey line 1 with three different background conductivities ranging from $5 \cdot 10^{-2}$ S/m to $5 \cdot 10^{-1}$ S/m. As the background geology becomes more conductive, the sensitivity sharply decreases. The loss of the sensitivity is explained by the fact that in more conductive background, casing tends to leak more currents horizontally and limits the flow of the currents to HAFZ. In general, the top-casing electrical source method may not work well in highly conductive earth environments. However, we have found that the presence of oil-based mud has potential to improve the sensitivity of the top-casing electric source method even in a conductive environment, because the mud is highly resistive up to 1,000 Ohm-m and reduces leaking current from the well (Jannin et al., 2018). To examine the effect of the oil-based mud on the sensitivity, we assume that the L-shaped well (**Figure** 5) is coated with 0.2m thick, 100 Ohm-m oil-based mud and compute the surface electric field responses to the factures in two conductive ($5 \cdot 10^{-2}$ and $5 \cdot 10^{-1}$ S/m) background models (**Figure** 11). The comparison of **Figures** 10 and 11 shows that the presence of thin oil-based mud coating increases the sensitivity of the method by about 80%, demonstrating the potential benefit of oil-based mud for the top-casing source method for detecting deep HAFZ in a conductive environment.

INVERSE SENSITIVITY OF TOP-CASING ELECTRIC SOURCE METHOD TO HAFZ

In this section, we examine the imaging sensitivity to the four HAFZ models (**Figure** 6 and **Table** 1) as the final step of proof-of-concept studies for the top-casing electrical source method. To ensure the detection sensitivity to HAFZ, we assume that the background geology is resistive enough (i.e. $5 \cdot 10^{-3}$ S/m) such that the electrical currents can flow through the casing without significant leakage. The Permian Basin and the Marcellus shale can be considered such resistive. We also assume that the cased well is homogeneous and continuous. In addition, we adapt two extra assumptions from Hoversten et al. (2017) that (1) electric field measurements are contaminated with 1% error of their amplitudes and (2) electric field noise floor is 10^{-10} V/m. The four assumptions might not always be satisfied in practice.

However, the consideration about their potential influences is avoided in this study to focus on the basic imaging capabilities of the top-casing electrical methods for HAFZ.

Figure 12 summarizes the imaging experiment over HAFZ model 1. The starting model is a $5 \cdot 10^{-3}$ S/m homogeneous half-space. An imaging domain covers 0≤*x*≤400, -1000≤*y*≤1000 and 1000≤*z*≤2000m. In other words, we assume that HAFZ resides inside the volume defined by the imaging domain. The L-BFGS-based imaging algorithm implemented here work well and converges after 15 iterations. The inversion is completed in 3 hours on 3.40GHz Intel Skylake processor with 64 GB memory. After the convergence, both observed and predicted data show good agreements. The inversion reasonably recovers the overall geometry of the HAFZ model 1 on the *yz* plane at x=200m (**Figure** 12a) although some scattered artifacts are seen on the *xz* plane at y=0m (**Figure** 12b).

Note that the boundaries of the recovered HAFZ are not smooth but somewhat irregular. This is because we use a relatively small regularization parameter in our inversion. A proper small regularization parameter is empirically determined via trial errors. It is our experience that a traditional cooling method with a large starting regularization parameter often smooths out a thin HAFZ structure in early inversion stages and fails to recover the fracture geometry in late stages with a small parameter. Accordingly, choosing a small starting regularization parameter is our practical choice for imaging thin HAFZ when a smooth background conductivity model is determined by other geophysical methods (e.g. Um et al., 2014).

In the experiment above, our imaging domain does not cover the entire modeling volume. We have found out that such a large imaging domain often leads to non-geological imaging results (e.g. highly scattered conductive structures). Instead, our imaging domain covers the horizontal well area with sufficient room for fracture developments in both lateral and vertical direction. While our proof-of-concept studies assume that the HAFZ is perpendicular to the well, realistic scenarios may involve that its geometry changes over time. Therefore, 400-by-2000-by1000m volume of the imaging domain would be reasonable. However, knowledge of both the fluid injection location and the amount of the injected fluid helps us to estimate a possible maximum volume of the imaging domain (Hoversten et al., 2017). Coupled flow and geomechanics simulation for various scenarios with different geological media (Kim and Moridis, 2013) can further assist refining the imaging domain size.

MEQ analysis can also roughly tell us about the locations of fracturing events, helping us better define a volume of the imaging domain. Therefore, it is worth to perform imaging experiments with an MEQ-guided imaging domain. For example, we assume that by having MEQ analysis, we can reduce $0 \leq x \leq 400$ of the imaging domain to $175 \leq x \leq 225$m where we have an injection point at (x=200m, y=0m and z=1600m). The assumption is also reasonable from geomechanical perspectives because the domain size of 50m in the *x* direction would be sufficiently large such that HAFZ can contain both main fracture networks and small micro-fractures/fissures that can induce substantial leakage of injection fluid (Fisher and Warpinski, 2012). The other dimensions of the imaging domain keep the same as those used in **Figure** 12.

Figure 13 shows the imaging experiments for model 1 with the imaging domain constrained in the *x* direction. Although the thickness of HAFZ model 1 is still not clearly resolved but blurred, the width and the height of model 1 are slightly better resolved. The use of the tight imaging domain also prevents unrealistic scattered conductive structures on the *xz* plane at y=0m shown in **Figure** 12b. **Figures** 14-16 show the imaging experiments for the remaining three HAFZ models with the same constrained imaging domain. **Figures** 13-16 clearly show that the casing-top electrical method can effectively delineate systematical changes in the width and the height of HAFZ although it is still daunting to resolve the thickness even in the imaging domain constrained in its direction.

Our last inversion experiment examines the effects of a higher noise level on the imaging sensitivity. To do this, the noise level for model 1 increases from 1 to 5 %. All other inverse modeling parameters and the volume of the imaging domain keep the same as those used in **Figure** 13. **Figure** 17 summarizes the imaging experiment with the high noise level. The inversion algorithm performs well and its convergence is similar to the previous examples. Compared with the inversion result with 1% noise (**Figure** 13), the height of HAFZ is reasonably recovered, but the accuracy of the width is deteriorated. This inversion example illustrates the importance of data quality for accurately resolving the detailed geometry of HAFZ.

CONCLUSION

We have presented advanced 3D electrical resistivity modeling and imaging algorithms that utilize heterogeneous types of meshes. The coarse rectangular FD meshes are used in the imaging domain to facilitate visualization and analysis of imaging results, whereas the tetrahedral FE simulation meshes are used for efficiently and accurately discretizing a multi-scale earth model. Linear mapping operators based on volume-averaging provides a robust link between the two difference mesh topologies. The algorithms are well suited to modeling and inverting electric field measurements in the presence of a steel-cased well. We have shown that a steel-cased well can be replaced by a prism. This replacement reduces the computational cost without deteriorating the solution accuracy, making it possible to rapidly simulate electric field responses over a 3D earth model in the presence of a steel-cased well.

We have shown that the top-casing electrical method is sensitive to and can delineate a localized HAFZ in a shallow depth. The primary advantage of the proposed method is the fact that the method employs surface sources and receivers and thus does not require borehole occupancy and interruption to the normal operation of the wells. As a result, its data acquisition can be cheaper and less cumbersome. We have numerically shown that the top-casing electric source method has potential to image HAFZ. The imaging results can be improved if the imaging domain is constrained.

To evaluate the proof of concept for the top-casing electrical method, our feasibility studies focused on fairly simple 3D HAFZ models. Several assumptions were also made to render our studies simple. For example, HAFZ is relatively shallow. The properties of the background geology and the steel-cased well were assumed known. However, in practice, it may not be always straightforward to characterize a deep localized HAFZ. A baseline resistivity model should be determined before hydraulic fracturing operations. The casing properties are also often unknown and may need to be determined by inversion. Accordingly, we expect that there are still challenges to accurately characterize deep HAFZ in practice. However, the feasibility studies presented here is encouraging. When the top-casing source method is considered for imaging HAFZ, the challenges described above will be important research topics.

ACKNOWLEDGEMENT

APPENDIX. MAPPING MATRICES $\mathbf{M}_{FE2FD}$ and $\mathbf{M}_{FD2FE}$

The mapping processes from FD to FE meshes are casted into

$$\boldsymbol{\sigma}^{FE} = \mathbf{M}_{\mathrm{FD2FE}}\boldsymbol{\sigma}^{FD}; \tag{A1}$$

(i,j) element of $\mathbf{M}_{\mathrm{FD2FE}ij} = \frac{1}{v_i^{FE}} \times (v_i^{FE} \cap v_j^{FD})$. (A2)

N_{FE}-by-N_{FD} matrix $\mathbf{M}_{FD2FE}$ is a mapping operator from FD to FE meshes. Vectors $\boldsymbol{\sigma}^{FE}$ and $\boldsymbol{\sigma}^{FD}$ contain conductivity attributes of the FE and FD models, respectively. v_i^{FE} and v_j^{FD} are the volume of the i^{th} FE element and the j^{th} FD element, respectively. The intersection operator $\cap$ computes the overlapping volume of the FE and FD cell if they intersect.

N_{FD}-by-N_{FE} matrix $\mathbf{M}_{FD2FE}$ is defined in the reverse way as shown below.

$$\boldsymbol{\sigma}^{FD} = \mathbf{M}_{\mathrm{FE2FD}}\boldsymbol{\sigma}^{FE}; \tag{A3}$$

(i,j) element of $\mathbf{M}_{\mathrm{FE2FD}ij} = \frac{1}{v_i^{FD}} \times (v_i^{FD} \cap v_j^{FE})$. (A4)

REFERENCES

Jannin, G., J. Chen, L. DePavia, L. Sun and M. Schwart, 2017, Deep electode: A game-changing technology for electromagnetic (EM) telemetry, Annual International Meeting, SEG, Expanded Abstracts, 1059-1062.

Commer, M., G. M. Hoversten, and E. S. Um, 2015, Transient-electromagnetic finite-difference time-domain earth modeling over steel infrastructure, Geophysics, **80**, E147-E162.

Commer, M., and G. A. Newman, 2008, New advances in three-dimensional controlled-source electromagnetic inversion, Geophysical Journal International, **172**, 513-535.

Commer, M. and G. A. Newman, 2004, A parallel finite-difference approach for 3D transient electromagnetic modeling with galvanic sources, Geophysics **69**, 1192-1202.

Cuevas, N., 2014, Analytical solutions of EM fields due to a dipole source inside an infinite casing, Geophysics, 79, E231-241.

Daneshy, A.A., 1973. On the Design of Vertical Hydraulic Fractures. SPE Journal of Petroleum Technology **25**, 83-97.

Davis, T.A., 2006, Direct methods for sparse linear systems, Society for Industrial and Applied Mathematics.

Egbert, G. D., and A. Kelbert, 2012, Computational recipes for electromagnetic inverse problems, Geophysical Journal International, **189**, 251-267.

Fisher, K., and N. Warpinski, 2012, Hydraulic fracture-height growth: real data. SPE Prod. Oper. **27**, 8-19

Grayver, A. V., 2015, Parallel three-dimensional magnetotelluric inversion using adaptive finite-element method. Part I: theory and synthetic study, Geophysical Journal International, **202**, 584-603.

Geertsma, J., and F. de Klerk, 1969. A Rapid Method of Predicting Width and Extent of Hydraulic Induced Fractures. J Pet Technol **2**, 1571-1581, SPE-2458-PA.

Gidley, J.L., S. A. Holditch, D. E. Nierode, W. Ralph, and R. W. Veatch, 1990, Recent advances in hydraulic fracturing. SPE Monograph Series Vol. **12**.

Hoversten, G. M., Commer, M., E. Haber, and C. Schwarzbach, 2015, Hydro-frac monitoring using ground time-domain electromagnetics, Geophysical Prospecting, **63**, 1508-1526.

Hoversten, M., C. Schawrzbach, E. Haber, P. Belliveau and R. Shekhtman, 2017, Borehole to surface electromagnetic monitoring of hydraulic fractures, 6th International Symposium on Three-Dimensional Electromagnetics, Berkeley, California, USA.

Jin, J.M., 2015, The finite element method in electromagnetics, 3rd edition, John Wiley & Sons.

Johnston, R. and J. Shrallow, 2011, Ambiguity in microseismic monitoring. Annual International Meeting, SEG, Expanded Abstracts, 1514-1518.

Kim, J. and G. J. Moridis, 2013, Development of the T+ M coupled flow–geomechanical simulator to describe fracture propagation and coupled flow–thermal–geomechanical processes in tight/shale gas systems. Computers & Geosciences, **60**, 184-198.

Kim, J., E. S. Um, and G. J. Moridis, 2014, Fracture propagation, fluid flow, and geomechanics of water-based hydraulic fracturing in shale gas systems and electromagnetic geophysical monitoring of fluid migration, SPE Hydraulic Fracturing Technology Conference, Society of Petroleum Engineers.

Marsala, A.F., A. D. Hibbs, and H. F. Morrison, 2014, December. Evaluation of Borehole Casing Sources for Electromagnetic Imaging of Deep Formations, International Petroleum Technology Conference.

Moridis, G.J. and C. M. Oldenburg, 2001, Process for guidance, containment, treatment, and imaging in a subsurface environment utilizing ferro-fluids (No. US 6250848), Lawrence Berkeley National Laboratory (LBNL), Berkeley, CA.

Newman, G.A. and D. L. Alumbaugh, 2000. Three-dimensional magnetotelluric inversion using non-linear conjugate gradients. Geophysical journal international, **140**, 410-424.

Nieuwemhuis, G., D. Yang, K. MacLennan, D. Oldenburg, M. Wilt and V. Ramadoss, 2015, Electrical imaging using a well casing as an antenna: a case study from a CO_2 sequestration site in Montana, American Geophysical Union Meeting.

Nocedal, J., and S. Wright, 2006, Numerical optimization, Springer Science & Business Media.

Nordgren, R.P., 1972. Propagation of a Vertical Hydraulic Fracture. SPE J. 12 (4): 306–314. SPE-3009-PA.

Patzer, C., K. Tietze, and O. Ritter, 2017, Steel-cased wells in 3-D controlled source EM modelling. Geophysical Journal International, **209**, 813-826.

Perkins, T.K., and L. R. Kern, 1961. Widths of Hydraulic Fractures. J Pet Technol, **13**, 937–949.

Puzyrev, V., E. Vilamajo, P. Queralt, J. Ledo, and A. Marcuello, 2016, Three-Dimensional Modeling of the Casing Effect in Onshore Controlled-Source Electromagnetic Surveys, Surveys in Geophysics, **38**, 527-545.

Rahmani, A.R., A. E. Athey, J. Chen, and M. J. Wilt, 2014, Sensitivity of dipole magnetic tomography to magnetic nanoparticle injectates, Journal of Applied Geophysics, ***103***, 199-214.

Schenkel, C.J. and H. F. Morrison, 1994. Electrical resistivity measurement through metal casing. Geophysics, **59**, 1072-1082.

Si, H., 2015, TetGen, a Delaunay-based quality tetrahedral mesh generator. ACM Transactions on Mathematical Software (TOMS), **4**, 11.

Tietze, K., O. Ritter, and P. Veeken, 2015, Controlled-source electromagnetic monitoring of reservoir oil saturation using a novel borehole-to-surface configuration, Geophysical Prospecting, 63, 1468-1490.

Um, E. S., J. M. Harris, and D. L. Alumbaugh, 2010. 3D time-domain simulation of electromagnetic diffusion phenomena: A finite-element electric-field approach. Geophysics, **75**, F115-F126.

Um, E. S., M. Commer, and G. Newman. 2014, A strategy for coupled 3D imaging of large-scale seismic and electromagnetic data sets: Application to subsalt imaging, Geophysics **79**, ID1-ID13.

Um, E. S., M. Commer, G. A. Newman, and G. M. Hoversten, 2015. Finite element modelling of transient electromagnetic fields near steel-cased wells. Geophysical Journal International, **202**, 901-913.

Um, E. S., S. Kim and H. Fu, 2017, A tetrahedral mesh generation approach for 3D marine controlled-source electromagnetic modeling, Computer and Geosciences, **100**, 1-9.

Vermylen, J.P. and M.D. Zoback. 2011. Hydraulic fracturing, microseismic magnitudes, and stress evolution in the Barnett Shale, Texas, USA. SPE Hydraulic Fracturing Technology Conference, The woodland, TX, 24 – 26 Jan. 2011.

Warpinski, N.R., R.C. Kramm, J.R. Heinze, and C.K. Waltman. 2005. Comparison of single- and dual-array microseismic mapping techniques in the Barnett shale. SPE ATCE, Dallas, TX, Oct. 9 – 12 2005.

Weiss, C. J., D. F. Aldridge, H. A. Knox, K. A. Schramm, and L. C. Bartel, 2016, The direct-current response of electrically conducting fractures excited by a grounded current source. Geophysics, **81**, E201-E210.

Weiss, C., 2017, Finite-element analysis for model parameters distributed on a hierarchy of geometric simplices, Geophysics, **82**, no. 4, E155-E167.

Yang, D., D. Oldenburg, and E. Haber, 2014, 3-D inversion of airborne electromagnetic data parallelized and accelerated by local mesh and adaptive soundings: Geophysical Journal International, **196**, 1942-1507.

Yang, D., and D. Oldenburg, 2016, Survey decomposition: A scalable framework for 3D controlled-source electromagnetic inversion: Geophysics, **81**, E69-E87.

Zoback M.D. 2007 Reservoir geomechanics. Cambridge, Cambridge university press.

Zoback, M., Kitasei, S., and Copithorne, B. 2010 Addressing the environmental risks from shale gas development. World Watch Institute Briefing Paper 1, World watch Institute (Washington DC)

FIGURE CAPTIONS

Figure 1. (a) 200m long hollow steel-cased well model. The air, the earth and the casing are set to $3 \cdot 10^{-7}$, $3 \cdot 10^{-2}$ and 10^{6} (S/m), respectively. (b) Its corresponding solid rectangular prism model.

Figure 2. Comparison of surface +*x*-oriented electric field responses to the two models (**Figure** 1).

Figure 3. *XY* cross-sectional views of 3D FD models with a conductivity color bar (log scale). (a) A 1km long vertical hollow steel-cased well. (b) A solid cylinder that has the same outer diameter of the hollow steel-cased well. (c) A rectangular prism of which its side length is equal to the diameter of the hollow steel-cased well. The earth and the casing are set to $3.33 \cdot 10^{-2}$ and $5 \cdot 10^{6}$ S/m, respectively. The cylinder and prism are set to $1.73 \cdot 10^{6}$ and $1.36 \cdot 10^{6}$ S/m, respectively. R_{in} and R_{out} represent the inner and outer radius of the casing, and W the width of the rectangular prism.

Figure 4. Comparison of DC responses to the true and approximate casing models shown in **Figure** 3. (a) Surface +*x*-oriented electric field responses. (b) Relative differences of the approximate model responses with respect to the hollow cased well model response.

Figure 5. A top-casing electric source configuration for detecting HAFZ at z=1.6 km and *x*=200m. *X*-oriented and *y*-oriented electric fields are measured along survey line 1 and 2, respectively.

Figure 6. The four hydraulically active fractured zone models. The *yz* cross-sectional view at *x*=200m (a) Model 1. (b) Model 2. (c) Model 3. (d) Model 4.

Figure 7. Electric field measurements along (a) survey line 1 and (b) survey line 2 and their relative difference with respect to the 0.005 S/m (200 Ohm-m) background response.

Figure 8. Electric field measurements without the steel-cased well along (a) survey line 1 and (b) survey line 2 and their relative difference with respect to the background response.

Figure 9. Electric field measurements along +x axis (survey line 1) with partially and fully damaged cased wells. (a) Intact ($5 \cdot 10^6$ S/m) casing (**Figure** 5a). (b)The corroded ($5 \cdot 10^3$ S/m) casing at z=500m. (c) The completely broken casing at z=500m.

Figure 10. Electric field measurements along +x axis (survey line 1) with different background conductivity values. (a) Background conductivity=$5 \cdot 10^{-2}$ S/m. (b) Background conductivity=$5 \cdot 10^{-1}$ S/m.

Figure 11. Electric field measurements along +x axis (survey line 1) with different background conductivity values. (a) Background conductivity=$5 \cdot 10^{-2}$ S/m. (b) Background conductivity=$5 \cdot 10^{-1}$ S/m. The cased well is coated with 0.2m thick 10^{-2} S/m oil-based mud.

Figure 12. Inversion for model 1. (a) *YZ* cross-sectional view at x=200m. (b) *XZ* cross-sectional view at y=0m. (c) Data plots along line 1 before and after the inversion. (d) Data plots along line 2 before and after the inversion. (e) Misfit as a function of inversion iteration. The white boxes in (a) and (b) indicate the true boundaries of model 1.

Figure 13. Inversion for model 1 with the imaging domain constrained in the x-direction. (a) *YZ* cross-sectional view at x=200m. (b) *XZ* cross-sectional view at y=0m. (c) Data plots along line 1 before and after the inversion. (d) Data plots along line 2 before and after the inversion. (e) Misfit as a function of inversion iteration. The white boxes in (a) and (b) indicate the true boundaries of model 1.

Figure 14. Inversion for model 2 with the imaging domain constrained in the x-direction. (a) *YZ* cross-sectional view at x=200m. (b) *XZ* cross-sectional view at y=0m. (c) Data plots along line 1 before and after the inversion. (d) Data plots along line 2 before and after the inversion. (e) Misfit as a function of inversion iteration. The white boxes in (a) and (b) indicate the true boundaries of model 2.

Figure 15. Inversion for model 3 with the imaging domain constrained in the x-direction. (a) *YZ* cross-sectional view at x=200m. (b) *XZ* cross-sectional view at y=0m. (c) Data plots along line 1 before and after the inversion. (d) Data plots along line 2 before and after the inversion. (e) Misfit as a function of inversion iteration. The white boxes in (a) and (b) indicate the true boundaries of model 3.

Figure 16. Inversion for model 4 with the imaging domain constrained in the x-direction.. (a) *YZ* cross-sectional view at x=200m. (b) *XZ* cross-sectional view at y=0m. (c) Data plots along line 1 before and after the inversion. (d) Data plots along line 2 before and after the inversion. (e) Misfit as a function of inversion iteration. The white boxes in (a) and (b) indicate the true boundaries of model 4.

Figure 17. Inversion for model 1 with 5% noise level. (a) *YZ* cross-sectional view at x=200m. (b) *XZ* cross-sectional view at y=0m. (c) Data plots along line 1 before and after the inversion. (d) Data plots along line 2 before and after the inversion. (e) Misfit as a function of inversion iteration.

FIGURES

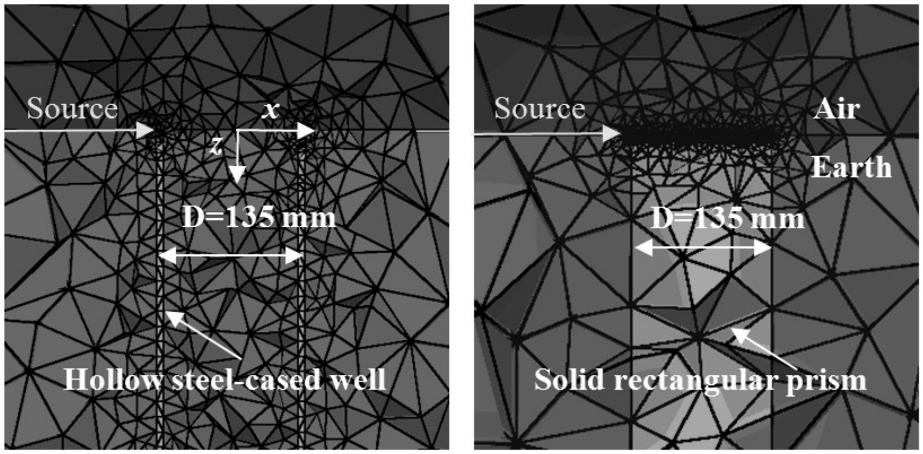

(a) (b)

Figure 1. (a) 200m long hollow steel-cased well model. The air, the earth and the casing are set to $3\cdot10^{-7}$, $3\cdot10^{-2}$ and 10^{6} (S/m), respectively. (b) Its corresponding solid rectangular prism model.

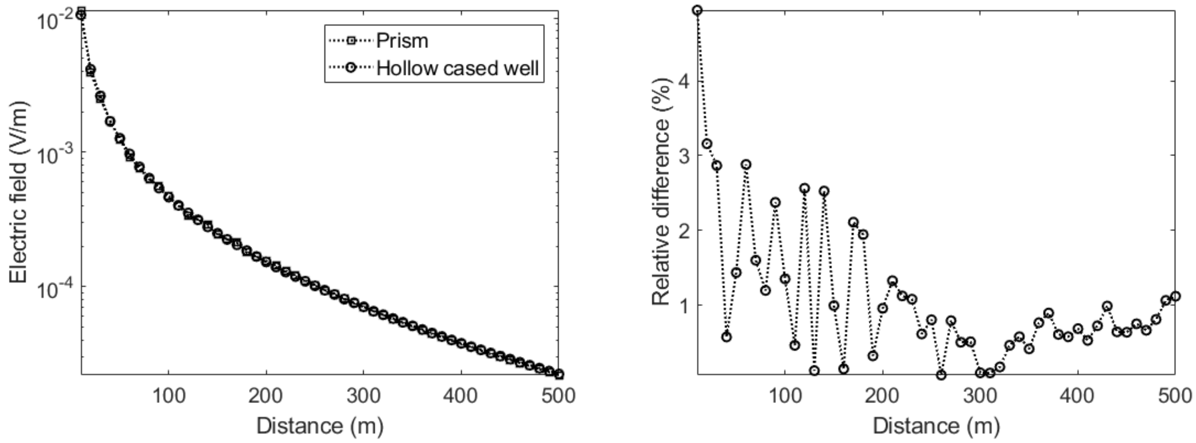

(a) (b)

Figure 2. Comparison of surface +*x*-oriented electric field responses to the two models (**Figure** 1).

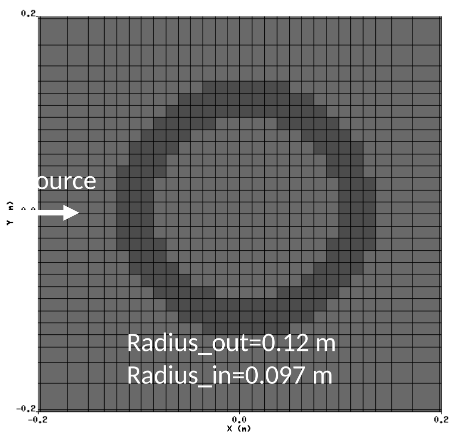

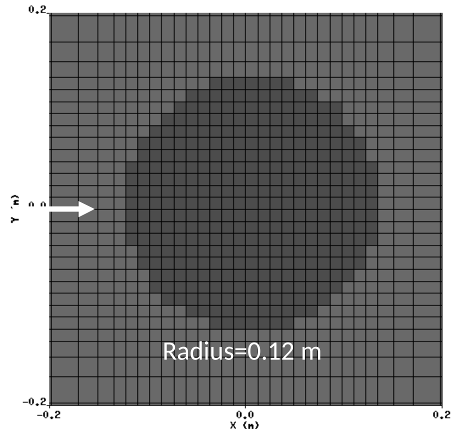

(a) (b)

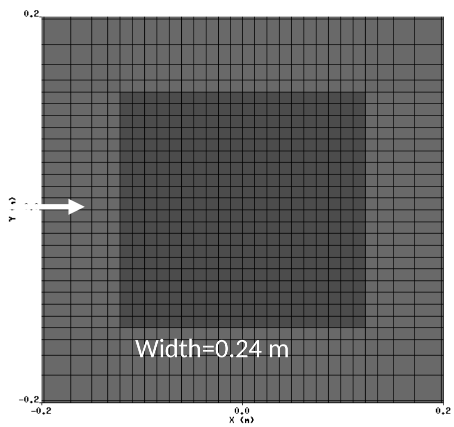

(c)

Figure 3. *XY* cross-sectional views of 3D FD models with a conductivity color bar (log scale). (a) A 1km long vertical hollow steel-cased well. (b) A solid cylinder that has the same outer diameter of the hollow steel-cased well. (c) A rectangular prism of which its side length is equal to the diameter of the hollow steel-cased well. The earth and the casing are set to $3.33 \cdot 10^{-2}$ and $5 \cdot 10^{6}$ S/m, respectively. The cylinder and prism are set to $1.73 \cdot 10^{6}$ and $1.36 \cdot 10^{6}$ S/m, respectively. R_{in} and R_{out} represent the inner and outer radius of the casing, and W the width of the rectangular prism.

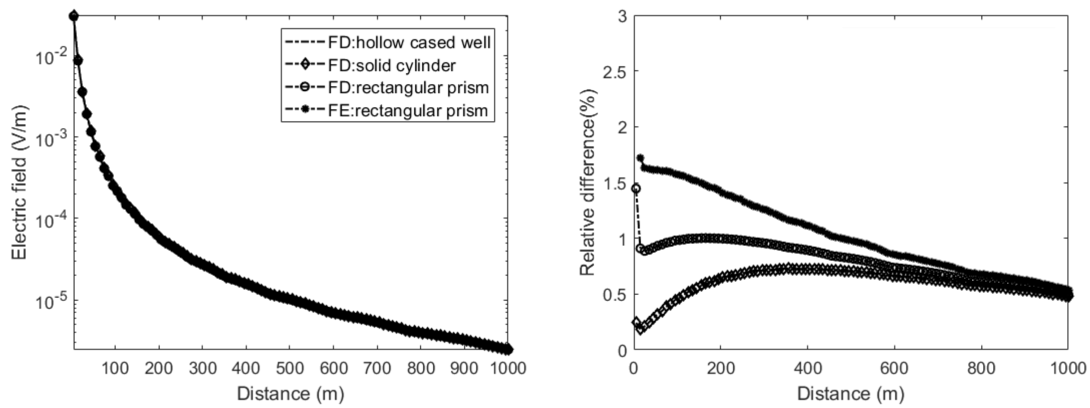

(a) (b)

Figure 4. Comparison of DC responses to the true and approximate casing models shown in **Figure** 3. (a) Surface +*x*-oriented electric field responses. (b) Relative differences of the approximate model responses with respect to the hollow cased well model response.

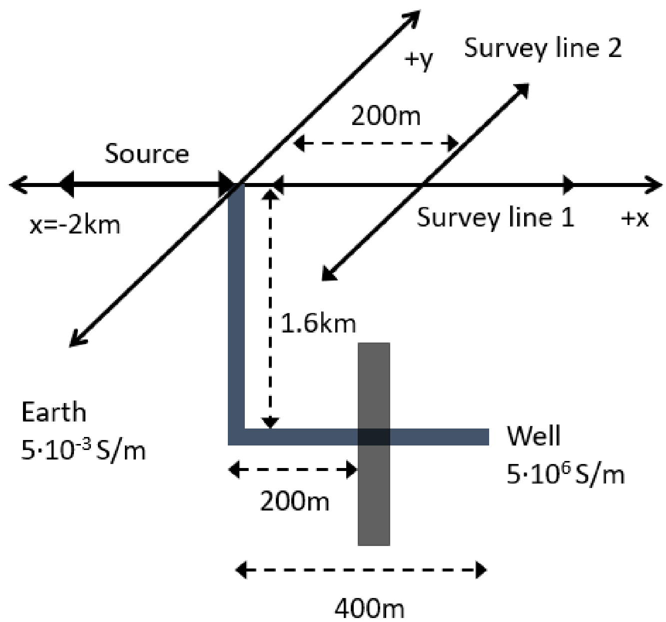

Figure 5. A top-casing electric source configuration for detecting HAFZ at z=1.6 km and *x*=200m. *X*-oriented and *y*-oriented electric fields are measured along survey line 1 and 2, respectively.

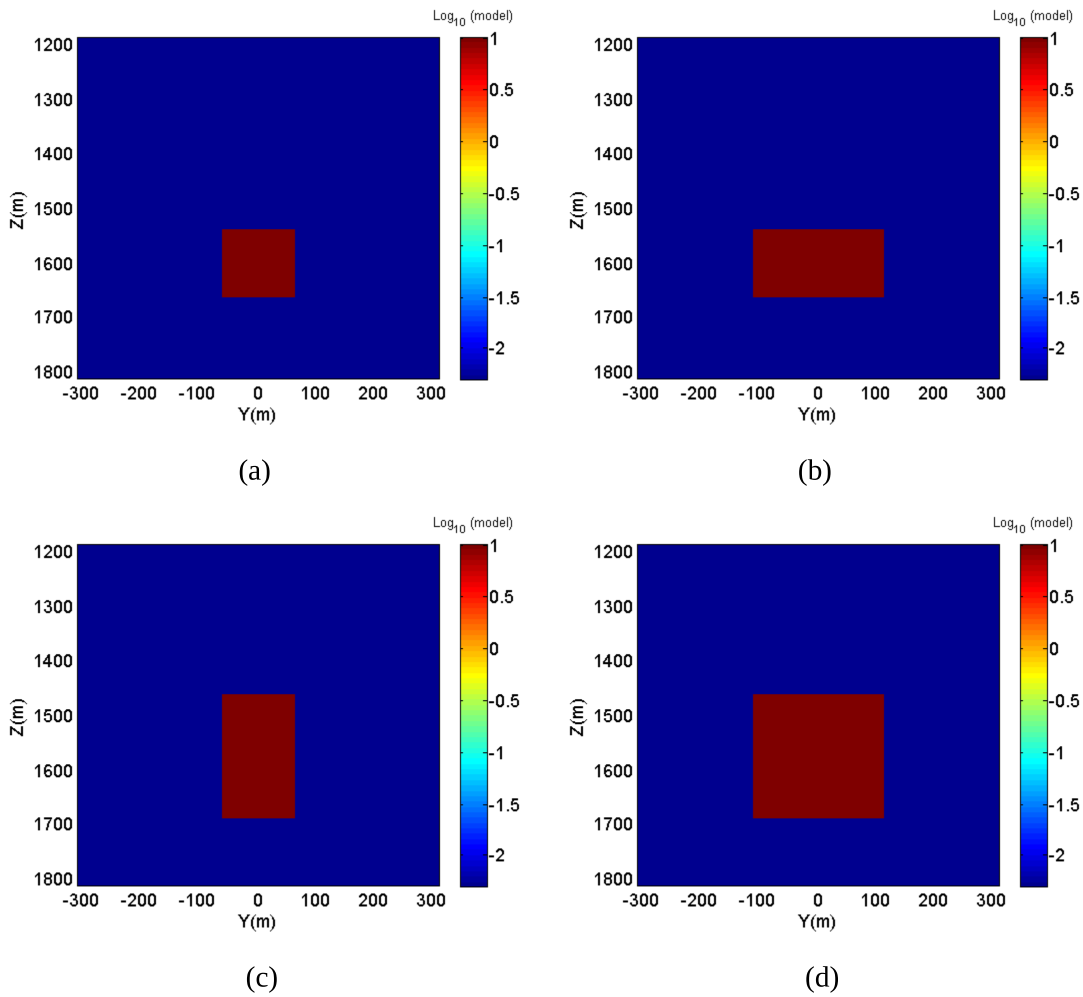

Figure 6. The four hydraulically active fractured zone models. The *yz* cross-sectional view at *x*=200m (a) Model 1. (b) Model 2. (c) Model 3. (d) Model 4.

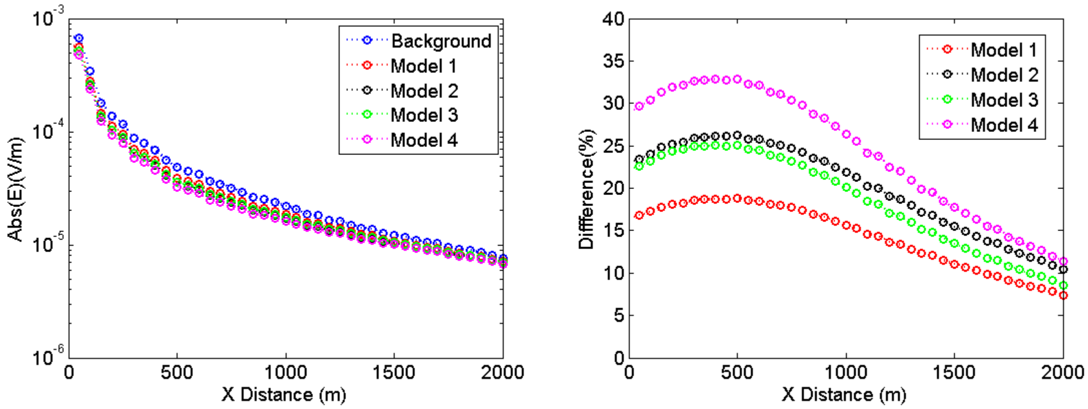

(a)

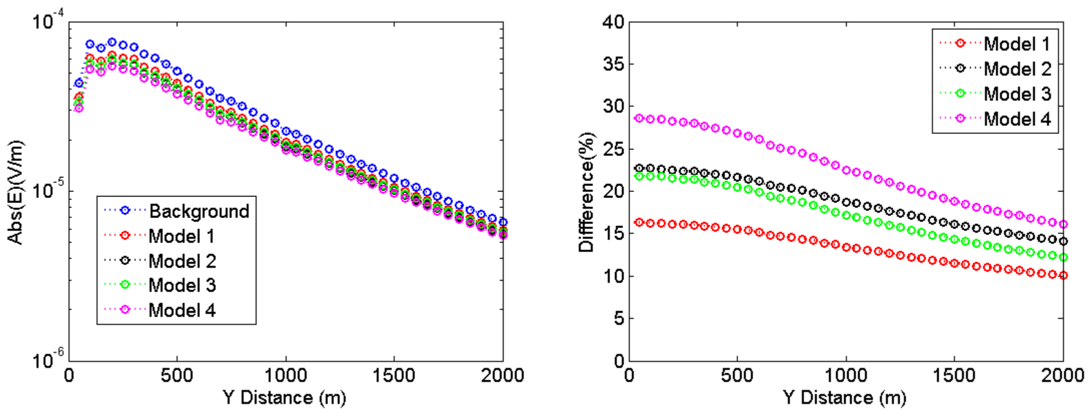

(b)

Figure 7. Electric field measurements along (a) survey line 1 and (b) survey line 2 and their relative difference with respect to the 0.005 S/m (200 Ohm-m) background response.

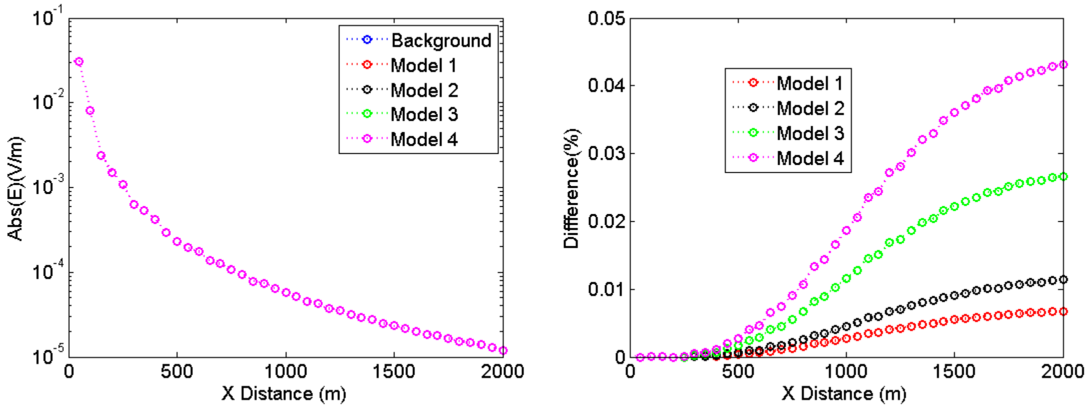

(a)

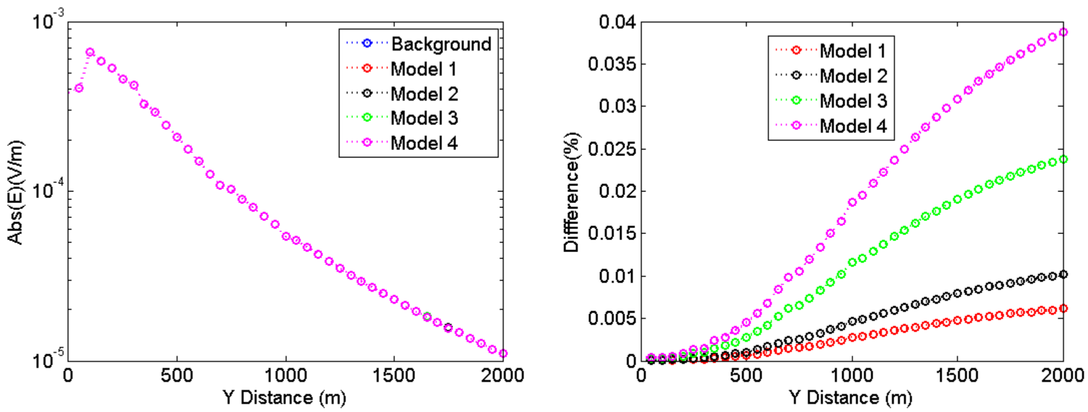

(b)

Figure 8. Electric field measurements without the steel-cased well along (a) survey line 1 and (b) survey line 2 and their relative difference with respect to the background response.

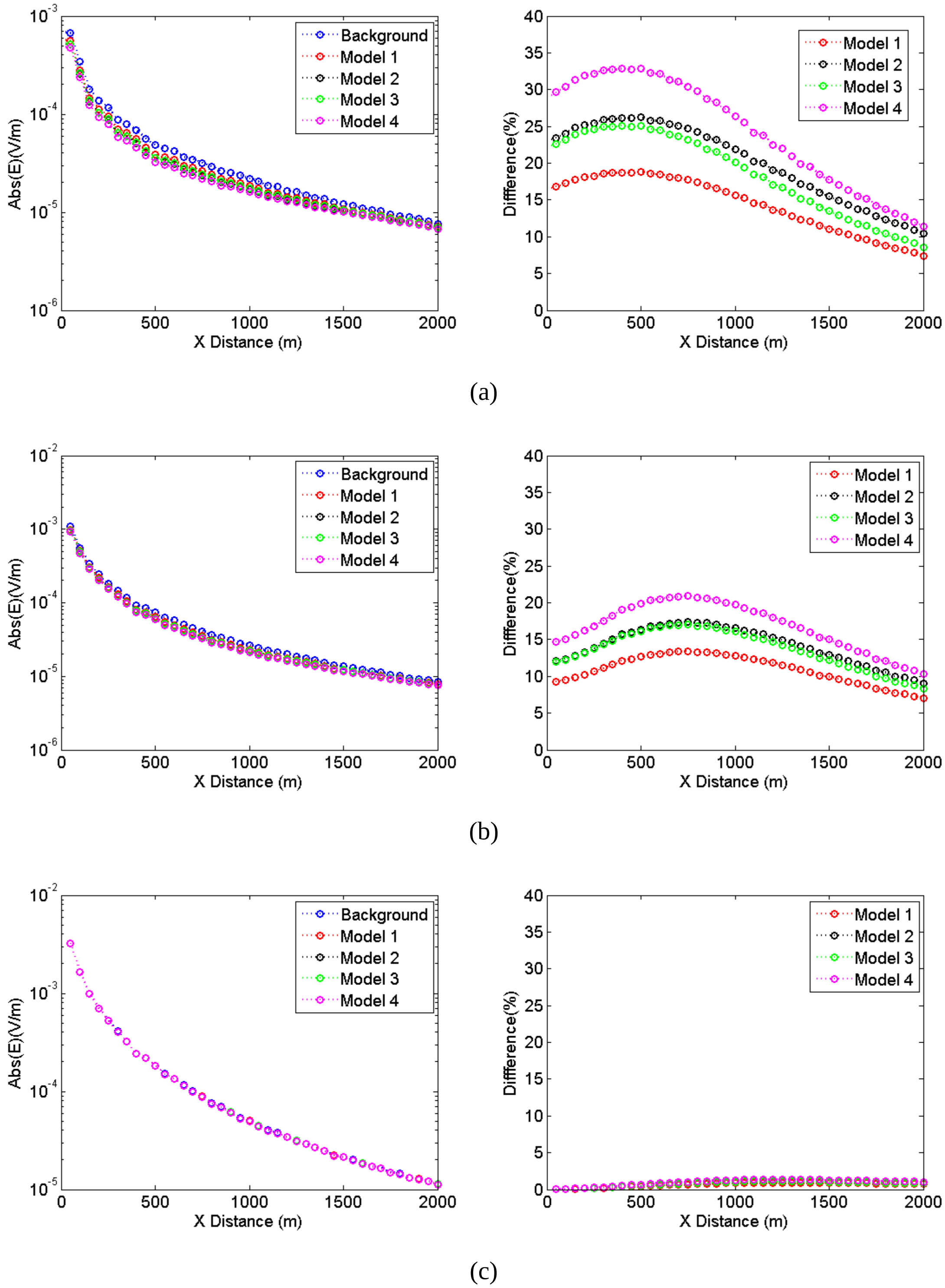

Figure 9. Electric field measurements along +x axis (survey line 1) with partially and fully damaged cased wells. (a) Intact ($5\cdot10^6$ S/m) casing (**Figure** 5a). (b)The corroded ($5\cdot10^3$ S/m) casing at z=500m. (c) The completely broken casing at z=500m.

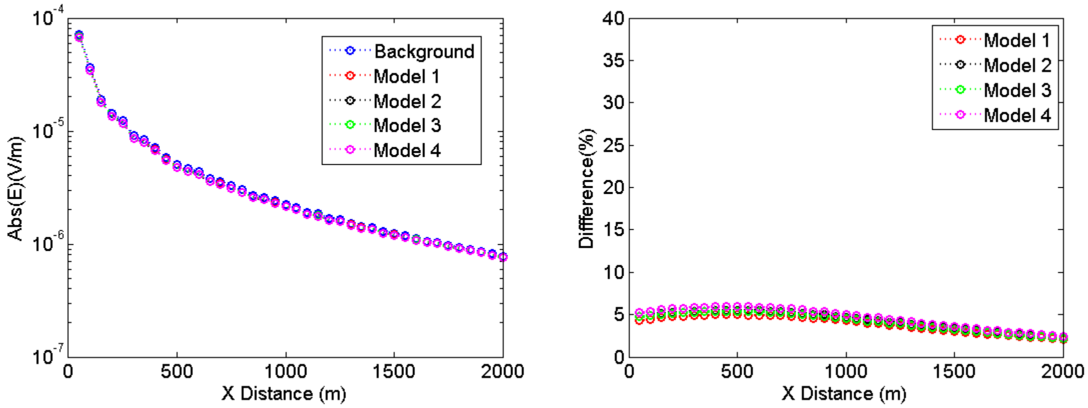

(a)

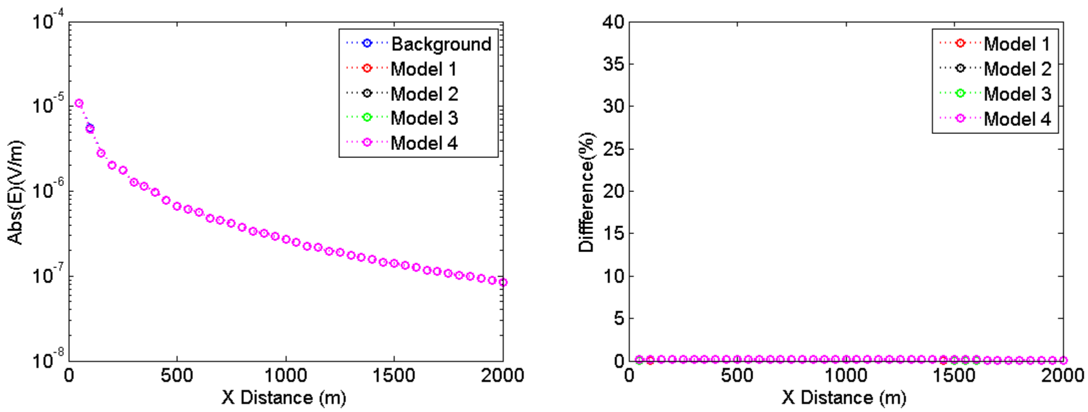

(b)

Figure 10. Electric field measurements along +x axis (survey line 1) with different background conductivity values. (a) Background conductivity=$5 \cdot 10^{-2}$ S/m. (b) Background conductivity=$5 \cdot 10^{-1}$ S/m.

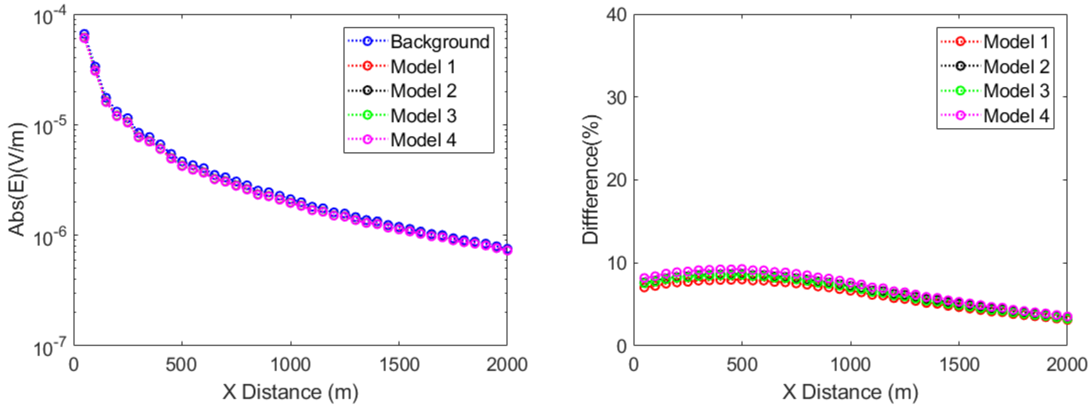

(a)

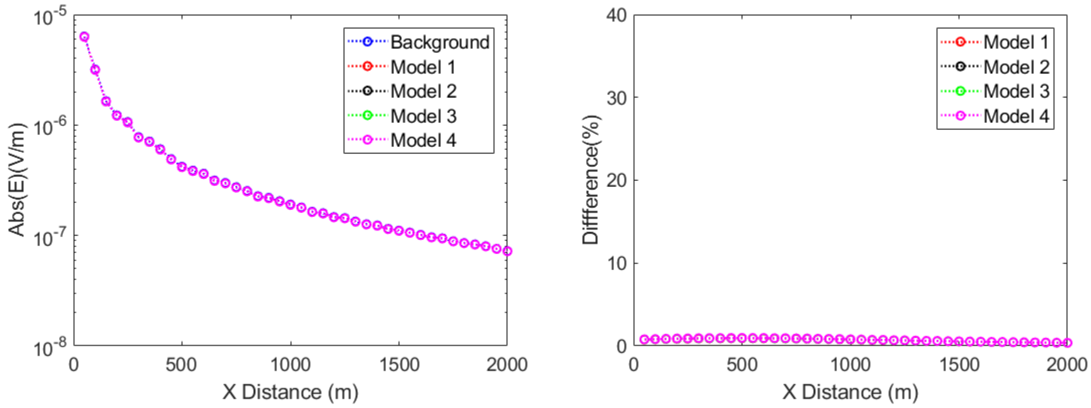

(b)

Figure 11. Electric field measurements along +x axis (survey line 1) with different background conductivity values. (a) Background conductivity=$5{\cdot}10^{-2}$ S/m. (b) Background conductivity=$5{\cdot}10^{-1}$ S/m. The cased well is coated with 0.2m thick 10^{-2} S/m oil-based mud.

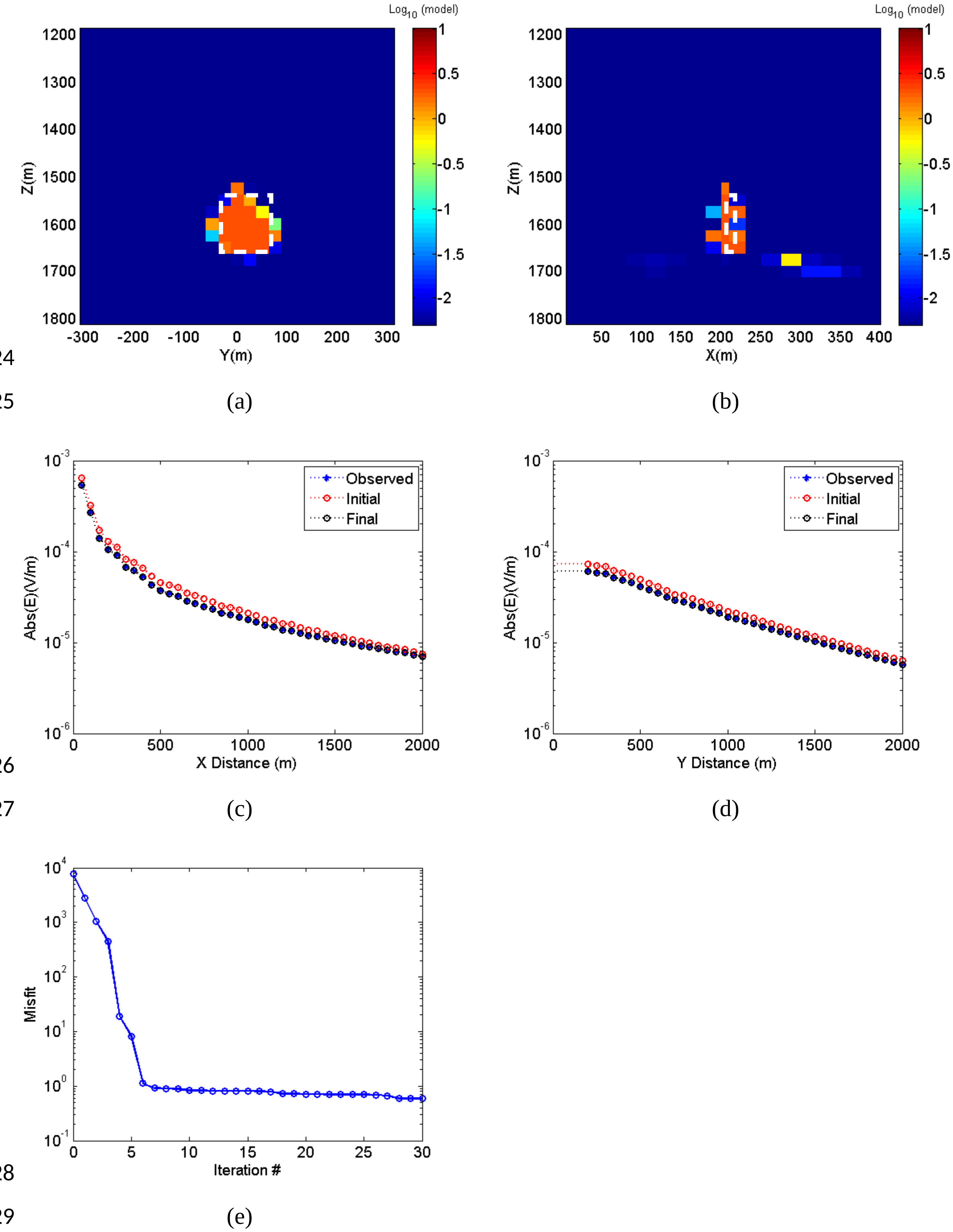

Figure 12. Inversion for model 1. (a) *YZ* cross-sectional view at x=200m. (b) *XZ* cross-sectional view at y=0m. (c) Data plots along line 1 before and after the inversion. (d) Data plots along line 2 before and after the inversion. (e) Misfit as a function of inversion iteration. The white boxes in (a) and (b) indicate the true boundaries of model 1.

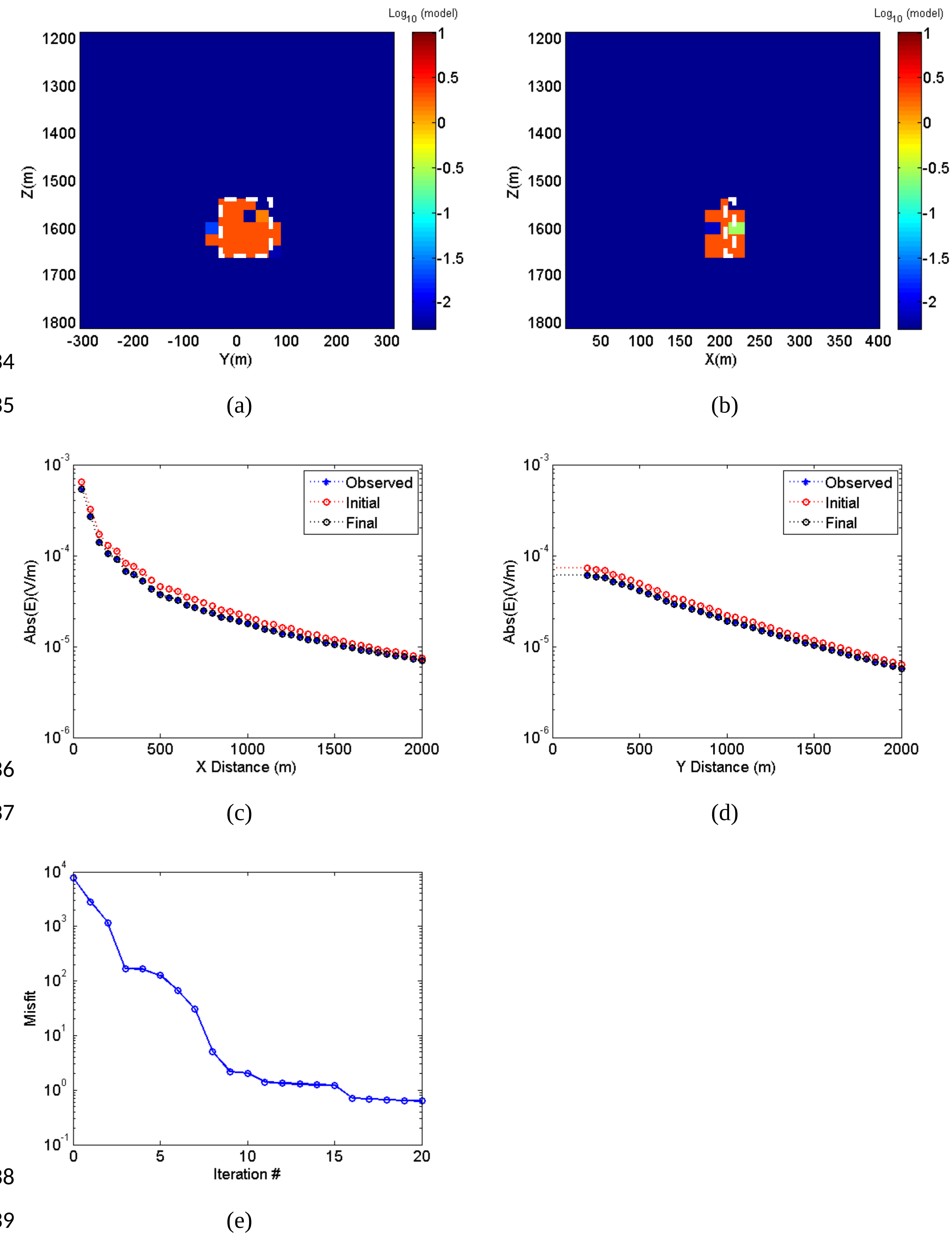

Figure 13. Inversion for model 1 with the imaging domain constrained in the x-direction. (a) *YZ* cross-sectional view at x=200m. (b) *XZ* cross-sectional view at y=0m. (c) Data plots along line 1 before and after the inversion. (d) Data plots along line 2 before and after the inversion. (e) Misfit as a function of inversion iteration. The white boxes in (a) and (b) indicate the true boundaries of model 1.

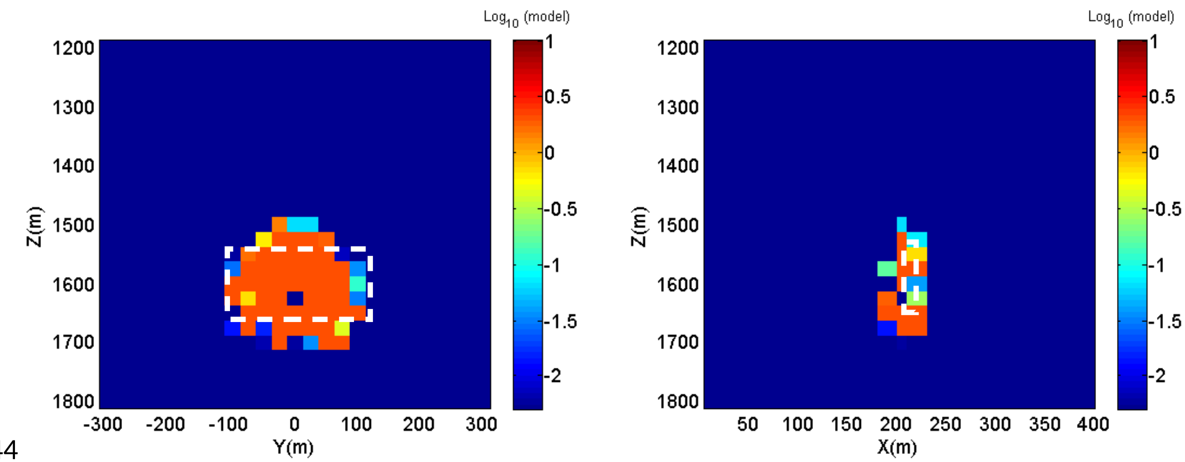

(a) (b)

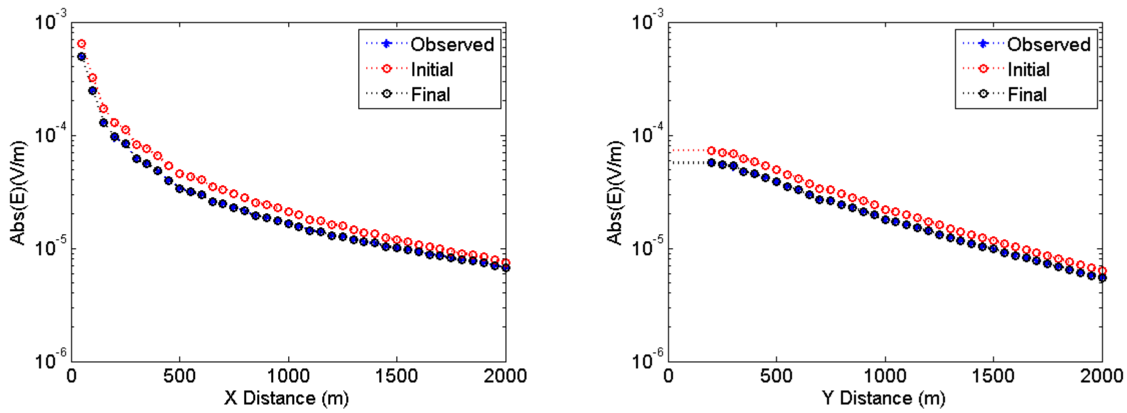

(c) (d)

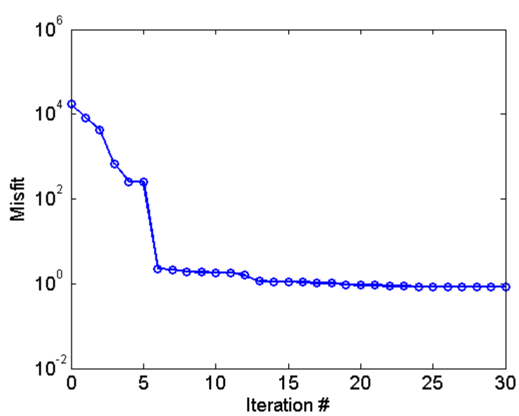

(e)

Figure 14. Inversion for model 2 with the imaging domain constrained in the x-direction. (a) *YZ* cross-sectional view at x=200m. (b) *XZ* cross-sectional view at y=0m. (c) Data plots along line 1 before and after the inversion. (d) Data plots along line 2 before and after the inversion. (e) Misfit as a function of inversion iteration. The white boxes in (a) and (b) indicate the true boundaries of model 2.

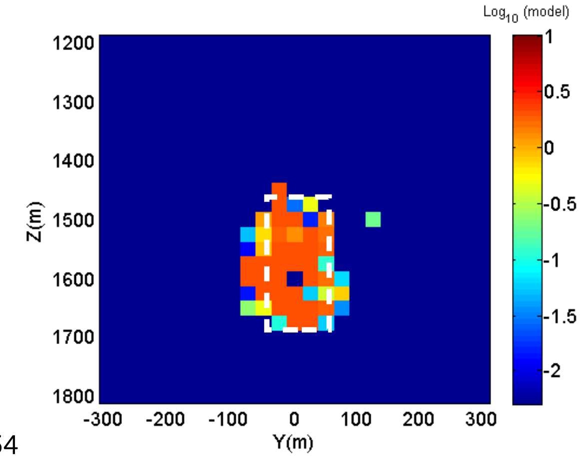

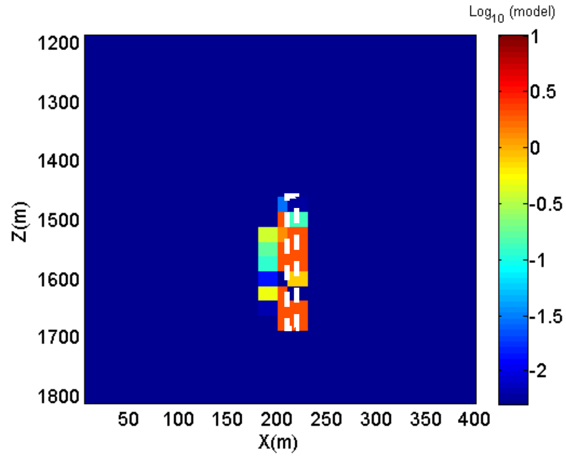

(a) (b)

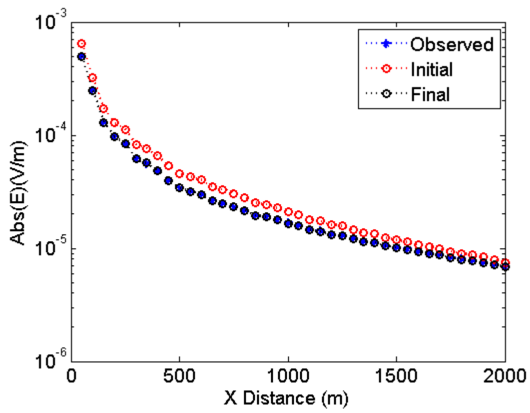

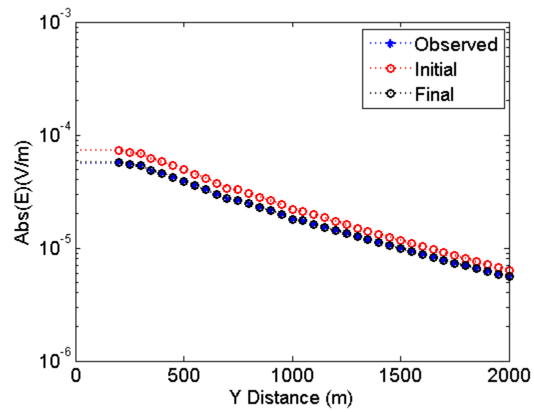

(c) (d)

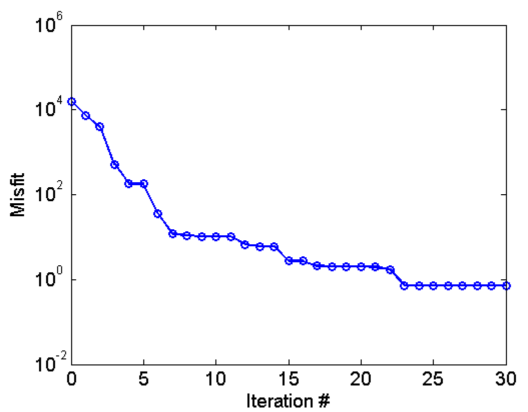

(e)

Figure 15. Inversion for model 3 with the imaging domain constrained in the x-direction. (a) *YZ* cross-sectional view at x=200m. (b) *XZ* cross-sectional view at y=0m. (c) Data plots along line 1 before and after the inversion. (d) Data plots along line 2 before and after the inversion. (e) Misfit as a function of inversion iteration. The white boxes in (a) and (b) indicate the true boundaries of model 3.

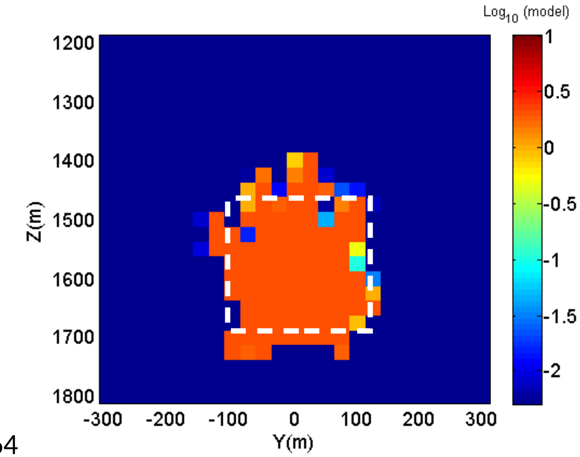

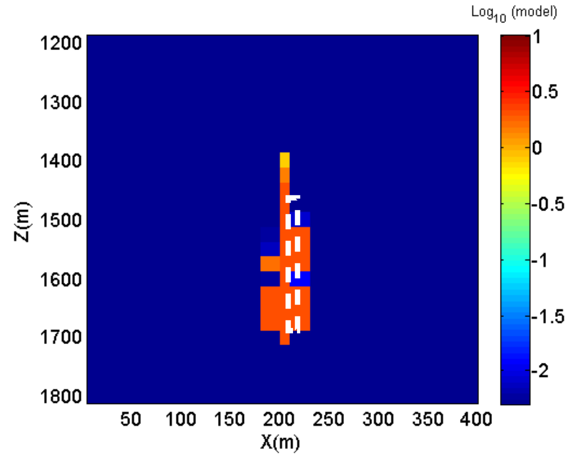

(a) (b)

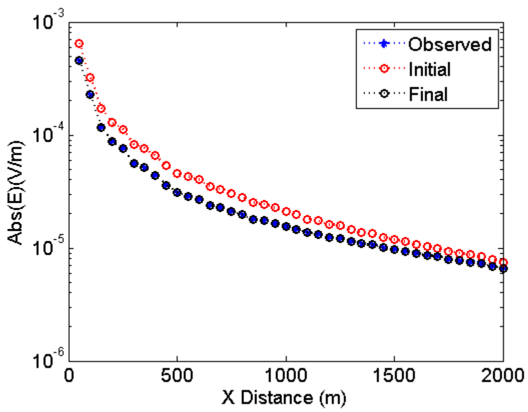

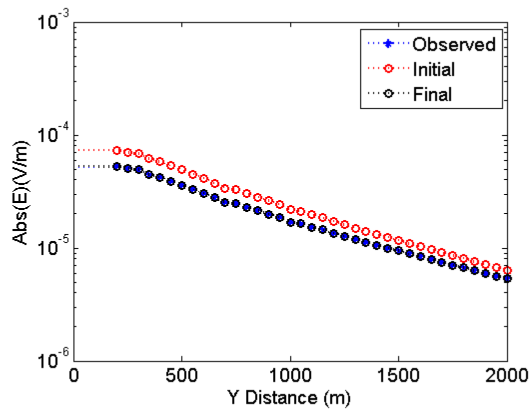

(c) (d)

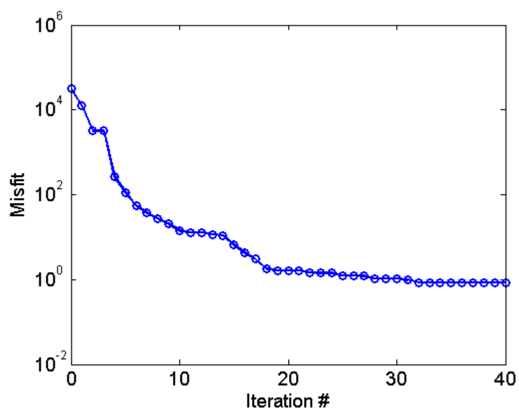

(e)

Figure 16. Inversion for model 4 with the imaging domain constrained in the x-direction.. (a) *YZ* cross-sectional view at x=200m. (b) *XZ* cross-sectional view at y=0m. (c) Data plots along line 1 before and after the inversion. (d) Data plots along line 2 before and after the inversion. (e) Misfit as a function of inversion iteration. The white boxes in (a) and (b) indicate the true boundaries of model 4.

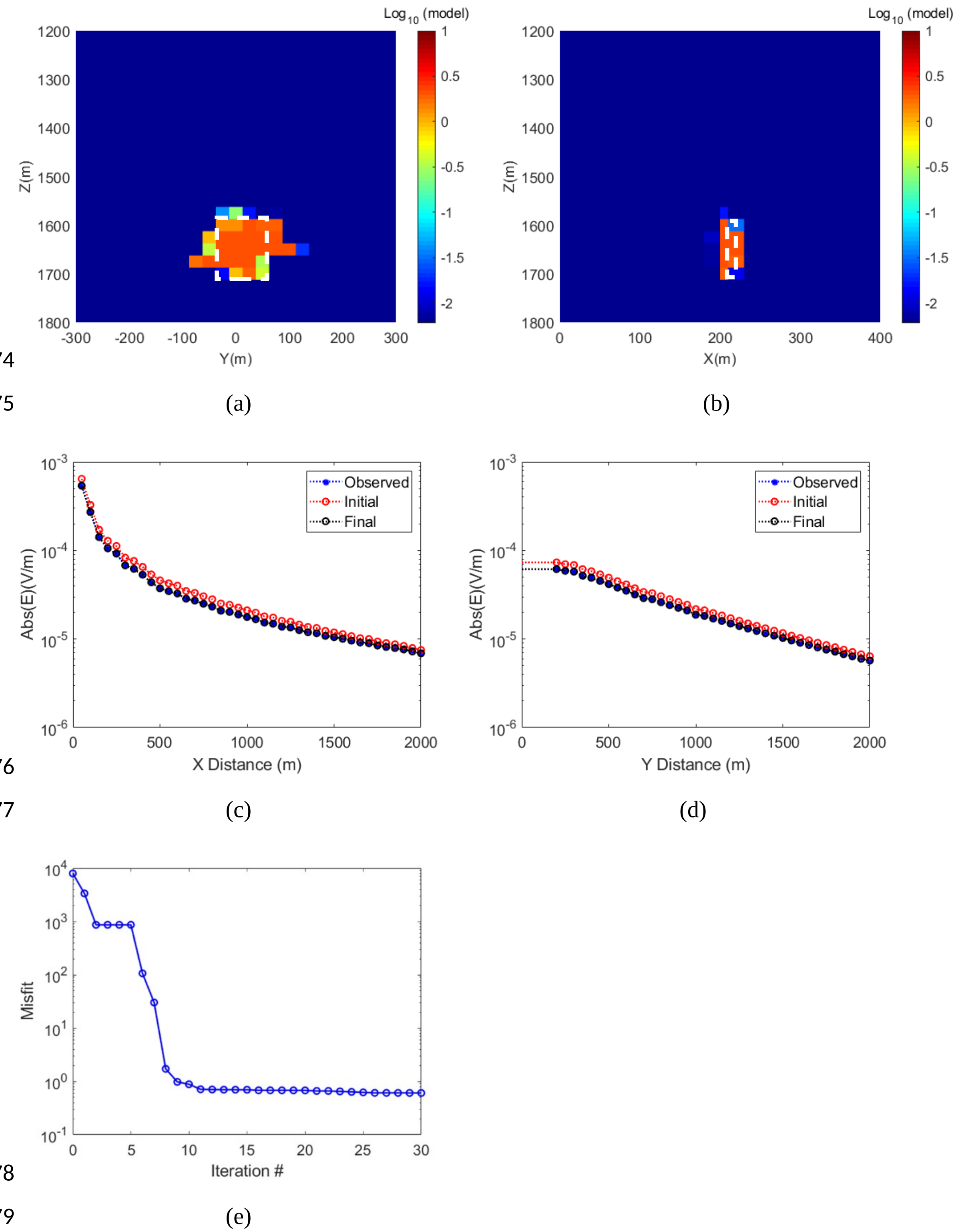

Figure 17. Inversion for model 1 with 5% noise level. (a) *YZ* cross-sectional view at x=200m. (b) *XZ* cross-sectional view at y=0m. (c) Data plots along line 1 before and after the inversion. (d) Data plots along line 2 before and after the inversion. (e) Misfit as a function of inversion iteration.

TABLE CAPTION

HAFZ	Width (m)	Height (m)	Thickness (m)	Conductivity (S/m)
Model 1	$-62.5 \le y \le 62.5$	$1537.5 \le z \le 1662.5$	$200 \le x \le 201$	10
Model 2	$-112.5 \le y \le 112.5$	$1537.5 \le z \le 1662.5$	$200 \le x \le 201$	10
Model 3	$-62.5 \le y \le 62.5$	$1462.5 \le z \le 1687.5$	$200 \le x \le 201$	10
Model 4	$-112.5 \le y \le 112.5$	$1462.5 \le z \le 1687.5$	$200 \le x \le 201$	10

Table 1. The description about the four HAFZ models.